Laguerre-Gaussian optical sum-sideband generation via orbital angular momentum exchange

Hao Xiong,* Ya-Min Huang, and Ying Wu
School of Physics, Huazhong University of Science and Technology, Wuhan, 430074, People's Republic of China

(Received 29 August 2020; revised 28 October 2020; accepted 24 March 2021; published 5 April 2021)

Laguerre-Gaussian optical sum-sideband generation via orbital angular momentum exchange has been studied analytically beyond the linearized approach. We obtain the analytical expression for the amplitudes of these signals within the semiclassical approximation. The pump power dependence of Laguerre-Gaussian sum-sideband generation is discussed, and we find that Laguerre-Gaussian sum-sideband generation can be remarkable even at low power through the satisfaction of matching conditions. The matching conditions for Laguerre-Gaussian sum-sideband generation in an optorotational system are discussed and summarized in detail, and the physical interpretation of matching conditions is discussed. The role of the topological charge value l on the sum-sideband generation is studied, which exhibits a saturation effect for the peak value of the normalized amplitude and consequently limits further improvement of the Laguerre-Gaussian sum-sideband generation. Our results may find applications in Laguerre-Gaussian optical frequency comb and communications and provide a potential method for the determination of the orbital angular momentum of light fields with high topological charges.

DOI: 10.1103/PhysRevA.103.043506

I. INTRODUCTION

The Laguerre-Gaussian (LG) beam, obtained as a type of eigensolution of the paraxial wave equation in cylindrical coordinates, possesses a helical phase structure and a doughnut-shaped intensity distribution with zero intensity at the beam center [1]. The LG beam carries an orbital angular momentum (OAM) of $l\hbar$ per photon along its propagation direction, with the integer l representing the azimuthal mode index or topological charge value [2]. Different methods such as computer-generated holograms [3,4], spiral phase plate or mirror [5,6], spatial light modulators (which may be the most common method to generate OAM modes in the laboratory) [7–9], and superposition of decentered Hermite-Gaussian beams [10], have been developed to generate a LG beam with well-defined orbital angular momentum.

Generation of an LG beam by spiral phase elements (such as spiral phase plates or spiral phase mirrors) may be the most straightforward approach [2]. The spiral phase plate is an optical element with a helical surface, and it can impart a well-defined orbital angular momentum to the photon reflected or transmitted [11]. The ability to convert a Gaussian mode into LG modes makes the spiral phase plate an important element in modern optics, and generation of LG beams with spiral phase elements is usually stable and efficient with respect to the other methods. The spiral phase plate and mirror can be fabricated with high precision and low mass, and the generation of LG beams with a topological charge value as high as 1000 has been demonstrated [12].

Recent experiments have been shown that LG beams can exert a torque on objects due to the transfer of orbital angular momentum, including microscopic absorptive particles [13], mesoscopic Bose-Einstein condensate [14], and submicron Brownian particle [15]. The torques arising in the spiral phase elements as a result of the interaction with light have been analyzed in Ref. [16], and a Laguerre-Gaussian optorotational system has been proposed, in analogy with the cavity optomechanical system [17,18]. The Laguerre-Gaussian optorotational system consists of two spiral phase elements acting as cavity mirrors [a schematic diagram is shown in Fig. 1(a)]. The input spiral phase element is rigidly fixed, and the Laguerre-Gaussian cavity modes can exchange an orbital angular momentum with the rear spiral phase mirror, which is able to rotate (treated as a torsional pendulum) along the intracavity axis [16].

Laguerre-Gaussian spiral phase systems with remarkable optorotational interaction have attracted great interest recently, and this emerging subject has led to many applications, including cooling of rotational mirrors [16], detection of orbital angular momentum of light fields [19,20], second-order sideband effects [21], and entanglements [22,23]. Due to the analogous Hamiltonian between the optorotational interaction and the optomechanical interaction [24,25], many effects arising from the optomechanical interaction [26–29] have corresponding analogs in the Laguerre-Gaussian optorotational system through the transfer of orbital angular momentum [19,21], which opens up fascinating possibilities for employing the orbital angular momentum states of light instead of momentum states.

In the present work, we consider that the Laguerre-Gaussian optorotational system is driven by a strong control field with the frequency ω_1 and two relatively weak probe fields with different frequencies (δ_a and δ_b, respectively, in a frame rotating at ω_1). Based on the nonlinear analytical method proposed previously [30], generation of Laguerre-Gaussian spectral components at the sum sideband [31,32] [with frequency $\pm(\delta_a + \delta_b)$ in a frame rotating at ω_1, as shown

*haoxiong1217@gmail.com

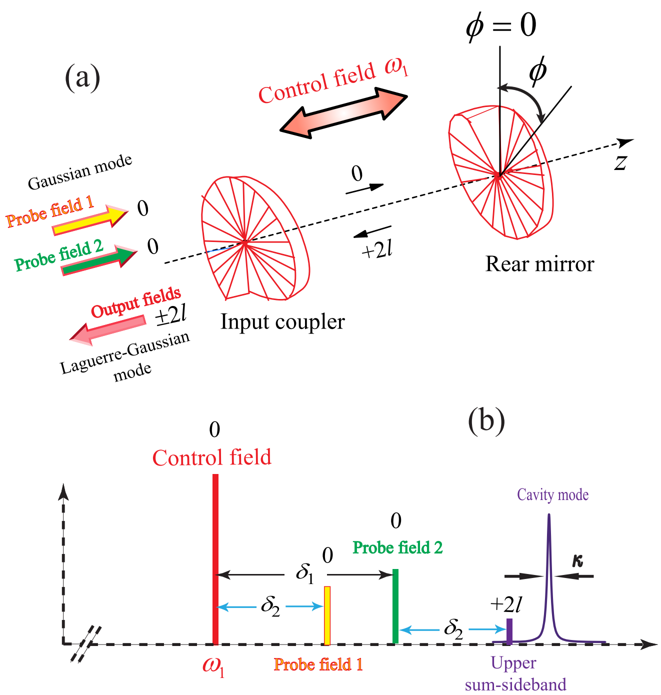

FIG. 1. (a) Schematic diagram of the Laguerre-Gaussian optical sum-sideband generation using angular momentum exchange. The optorotational system consists of two spiral phase elements in which the input coupler is rigidly fixed and the rear mirror is able to rotate (treated as a torsional pendulum) about the intracavity axis. The optorotational system is driven by a control field (with the frequency ω_1) and two probe fields (with frequencies ω_a and ω_b, respectively). (b) Frequency spectrogram of the Laguerre-Gaussian optical sum-sideband generation. When the control field and two probe fields (Gaussian beams with charge 0) are incident upon the optorotational system, there are output fields with frequencies $\pm(\delta_a + \delta_b)$ in a frame rotating at ω_1 generation (Laguerre-Gaussian beams with charge $2l$). In a frame rotating at ω_1, this process is very similar to sum frequency generation in a nonlinear medium.

in Fig. 1(b)] is discussed, including the the pump power dependence and the role of the topological charge value l. Although the amplitudes of Laguerre-Gaussian sum sideband generation are often small due to the weak optorotational coupling, the efficiencies of sum sideband generation can be enhanced significantly when the suitable matching conditions are met. The physical interpretation of these matching conditions is discussed in detail.

The signals of Laguerre-Gaussian sum-sideband generation may be important in understanding nonlinear optics through the transfer of orbital angular momentum of light, where the optical nonlinearity enhancement arising from optorotational interactions is still an area of exploration, especially with multiple driven optical interactions. Further developments in this direction may lead to interesting effects by introducing strong coupling of Laguerre-Gaussian optorotational system with other physical entities, such as phonons and magnons [33–37]. From the precision measurement perspective [38,39], matching conditions of the Laguerre-Gaussian sum sideband generation may provide a potential method for the determination of the orbital angular momentum of light fields with high topological charge, which play a crucial role in optical communications and encoding information using the optical orbital angular momentum. Further analysis is required to move in that direction.

This paper is organized as follows. We give an analytic description of the optorotational system in Sec. II, where the Hamiltonian formulation and a group of nonlinear evolution equations are given and simplified within the semiclassical approximation. We solve these nonlinear evolution equations analytically with suitable nonlinear ansatz, and the amplitudes of sum-sideband generation are obtained. In Sec. III, we discuss in detail the features of Laguerre-Gaussian sum-sideband generation in an optorotational system, including the pump power dependence, matching conditions, and the role of the topological charge value l on the sum-sideband generation. The matching conditions for Laguerre-Gaussian sum-sideband generation are summarized, and the physical interpretation of matching conditions are discussed. Finally, a conclusion of the results are summarized in Sec. IV.

II. ANALYTIC SOLUTIONS FOR THE LAGUERRE-GAUSSIAN SUM-SIDEBAND GENERATION IN AN OPTOROTATIONAL SYSTEM

A Laguerre-Gaussian optorotational system consisting of two spiral phase elements is shown schematically in Fig. 1(a). The input coupler is designed to be partially transparent such that it removes a fixed topological charge $2l$ from the laser beam upon reflection from either side of the spiral phase element, while allowing beams to pass through with no change to their topological charge due to the opposite winding on each side of the element. The rear mirror is designed to be perfectly reflective and it adds a topological charge $2l$ to the reflected beam [16]. We consider that the optorotational system is driven by a strong control field with the frequency ω_1 and two probe fields with frequencies ω_a and ω_b. All these input fields are Gaussian beams with the topological charge 0. The Hamiltonian formulation of the Laguerre-Gaussian optorotational system is [16]

$$\hat{H} = \hbar\omega_c\hat{a}^\dagger\hat{a} + \frac{\hat{L}_z^2}{2I} + \frac{I\omega_\phi^2}{2}\hat{\phi}^2 - \hbar g\hat{\phi}\hat{a}^\dagger\hat{a} + \hat{H}_{\text{control}} + \hat{H}_{\text{probe}},$$

where ω_c is the frequency of the cavity mode, $\hat{a}$ ($\hat{a}^\dagger$) is the bosonic annihilation (creation) operator of the cavity field, and $\hat{L}_z$ and $\hat{\phi}$ are the angular momentum operator and angular displacement operator of the rear mirror about the intracavity axis, respectively, satisfying the commutation relation $[\phi, L_z] = i\hbar$. I is the moment of inertia of the rotation mirror, ω_ϕ is the angular frequency of the rotational mirror described by a torsional pendulum, and $g = cl/L$ is the optorotational coupling parameter with c being the speed of light in vacuum. $\hat{H}_{\text{control}} = i\hbar\sqrt{\eta_c\kappa}s_1(\hat{a}^\dagger e^{-i\omega_1 t} - \hat{a}e^{i\omega_1 t})$ describes the incident coupling between the strong control field and the intracavity field with the coupling parameter $\eta_c = 1/2$, and $\hat{H}_{\text{probe}} = i\hbar\sqrt{\eta_c\kappa}(\hat{a}^\dagger s_a e^{-i\omega_a t} + \hat{a}^\dagger s_b e^{-i\omega_b t} - \hat{a}s_a^* e^{i\omega_a t} - \hat{a}s_b^* e^{i\omega_b t})$ describes the similar incident process with two probe fields with different frequencies (ω_a and ω_b, respectively). $s_i = \sqrt{P_i/\hbar\omega_i}$ ($i = 1,\ a,\ b$) are the normalized amplitudes of the input fields with P_1 being the pump power of the control field and P_a (P_b) being the power of the probe field with frequency ω_a (ω_b), respectively.

Based on the Hamiltonian, the Heisenberg-Langevin equations in a frame rotating at ω_1 read

$$\left(\frac{d}{dt}+\hat{A}\right)\hat{a}=\sqrt{\eta_c\kappa_a}\left(s_1+\sum_{i=a,b}s_ie^{-i\delta_it}\right)+\sqrt{\eta_c\kappa_a}\hat{a}_{\text{in}},$$
$$\frac{d^2\hat{\phi}}{dt^2}+\kappa_\phi\frac{d\hat{\phi}}{dt}+\omega_\phi^2\hat{\phi}=\frac{\hbar g}{I}\hat{a}^\dagger\hat{a}+\hat{F}_{\text{th}}, \tag{1}$$

where $\hat{A}=\kappa_a/2-i\Delta-ig\hat{\phi}$ with $\Delta=\omega_1-\omega_c$, $\delta_i=\omega_i-\omega_1$ ($i=a$, b), the noise operators of the cavity and torsional pendulum ($\hat{a}_{in}$ and $\hat{F}_{\text{th}}$) satisfy the correlation functions $\langle\hat{a}_{\text{in}}(t)\hat{a}_{\text{in}}^\dagger(t')\rangle=\delta(t-t')$, $\langle\hat{a}_{\text{in}}(t)\rangle=0$, $\langle\hat{F}_{\text{th}}(t)\hat{F}_{\text{th}}^\dagger(t')\rangle=\kappa_\phi\int e^{-i\omega(t-t')}[\coth(\hbar\omega/2k_BT)+1]d\omega/2\pi\omega_\phi$ and $\langle\hat{F}_{\text{th}}(t)\rangle=0$, and the decay rates of the cavity field (κ_a) and torsional pendulum (κ_ϕ) are introduced classically. Here, we focus on the mean response of the intracavity field to the probe fields, so the operators in the Heisenberg-Langevin equations (1) can be reduced to their expectation values, viz. $a(t)\equiv\langle\hat{a}(t)\rangle$, $a^*(t)\equiv\langle\hat{a}^\dagger(t)\rangle$, and $\phi(t)\equiv\langle\hat{\phi}(t)\rangle$. In this case, the evolution equations of the Laguerre-Gaussian optorotational system then become

$$\frac{d}{dt}a=(i\Delta+ig\phi-\kappa_a/2)a+\sqrt{\eta_c\kappa_a}\left(s_1+\sum_{i=a,b}s_ie^{-i\delta_it}\right),$$
$$I\left(\frac{d^2}{dt^2}+\omega_\phi^2+\kappa_\phi\frac{d}{dt}\right)\phi=\hbar ga^*a, \tag{2}$$

where the noise terms are dropped and the mean-field approximation by factorizing averages is used.

To solve the evolution equations of the Laguerre-Gaussian optorotational system, we assume that the control field is much stronger than the two probe fields, and the solution of the evolution equations can be written in the series form:

$$a=a_0+a_a^+e^{-i\delta_at}+a_a^-e^{i\delta_at}+a_b^+e^{-i\delta_bt}+a_b^-e^{i\delta_bt}+a_s^+e^{-i\Omega t}+a_s^-e^{i\Omega t}+\cdots,$$
$$\phi=\phi_0+\phi_ae^{-i\delta_at}+\phi_a^*e^{i\delta_at}+\phi_be^{-i\delta_bt}+\phi_b^*e^{i\delta_bt}+\phi_se^{-i\Omega t}+\phi_s^*e^{i\Omega t}+\cdots, \tag{3}$$

where $\Omega=\delta_a+\delta_b$ is the sum frequency in a frame rotating at ω_1, $a_0=-\sqrt{\eta_c\kappa_a}s_1/(i\Delta+ig\phi_0-\kappa_a/2)$ and $\phi_0=\hbar ga_0^*a_0/I\omega_\phi^2$ are the steady-state solutions provided by the control field. The frequency components of $\pm\Omega$ are the so-called sum sideband. In the perturbative regime, other frequency components, such as second-order and higher order sidebands, contribute little to sum-sideband generation due to the weak nonlinearity and are ignored in the ansatz (3). Here, we use the traditional terms, upper and lower sum sideband, to represent the frequency components $+\Omega$ and $-\Omega$, respectively [30]. Substitution of the ansatz with sum-sideband generation into Eqs. (2), we can obtain the following algebraic equations:

$$\frac{I}{\hbar g}(\omega_\phi^2-\Omega^2-i\kappa_\phi\Omega)\phi_s=a_0(a_s^-)^*+a_0^*a_s^++a_a^+(a_b^-)^*+a_b^+(a_a^-)^*,$$
$$(\kappa_a/2-i\Delta-ig\phi_0-i\Omega)a_s^+=ig(a_0\phi_s+a_a^+\phi_b+a_b^+\phi_a),$$
$$(\kappa_a/2-i\Delta-ig\phi_0+i\Omega)a_s^-=ig(a_0\phi_s^*+a_a^-\phi_b^*+a_b^-\phi_a^*), \tag{4}$$

where $a_i^+=s_i\tau(\delta_i)/[\theta(-\delta_i)\tau(\delta_i)-i\hbar g^2|a_0|^2]$ ($i=a$, b) with the functions $\theta(x)=\kappa_a/2-i\Delta-ig\phi_0+ix$, $\sigma(x)=I(\omega_\phi^2-x^2-i\kappa_\phi x)$, and $\tau(x)=\sigma(x)+i\hbar g^2|a_0|^2/[\theta(x)]^*$. $a_i^-=iga_0\phi_i^*/\theta(\delta_i)$, and $\phi_i=\hbar ga_0^*a_i^+/\tau(\delta_i)$. We note that, to obtain equations (4), the amplitude at the sum sideband is assumed to be much smaller than the two probe fields due to the fact that sum-sideband generation is a second-order process.

The solution to algebraic equations (4) gives the analytical expression for the Laguerre-Gaussian sum-sideband generation, and the amplitudes of sum-sideband generation in the optorotational system can be obtained as follows:

$$a_s^-=\frac{a_0\phi_s^*+a_a^-\phi_b^*+a_b^-\phi_a^*}{\theta(\Omega)/ig},\quad \phi_s=\frac{\hbar g}{\tau(\Omega)}(\wp+a_0^*a_s^+),$$
$$a_s^+=-\frac{(a_a^+\phi_b+a_b^+\phi_a)\tau(\Omega)+i\hbar g^2a_0\wp}{i\hbar g^2|a_0|^2-\theta(-\Omega)\tau(\Omega)}, \tag{5}$$

where $\wp=(a_a^-)^*a_b^++(a_b^-)^*a_a^+-iga_0[(a_a^-)^*\phi_b+(a_b^-)^*\phi_a]/[\theta(\Omega)]^*$. Using the input-output relation $s_{\text{out}}=s_{\text{in}}-\sqrt{\eta_c\kappa_a}a$, the amplitudes of the output field at upper and lower sum sidebands can be obtained as $-\sqrt{\eta_c\kappa_a}a_s^+$ and $-\sqrt{\eta_c\kappa_a}a_s^-$, respectively. To describe quantificationally the Laguerre-Gaussian sum-sideband generation process, we use the normalized amplitudes $|A_+|=\sqrt{\eta_c\kappa_a\hbar\omega_c|a_s^+|^2/P_0}$ and $|A_-|=\sqrt{\eta_c\kappa_a\hbar\omega_c|a_s^-|^2/P_0}$ with P_0 being an arbitrary power (here we choose $P_0=1$ mW for simplicity) to make $|A_+|$ and $|A_-|$ dimensionless.

III. FEATURES OF LAGUERRE-GAUSSIAN SUM-SIDEBAND GENERATION

The amplitudes of the Laguerre-Gaussian sum-sideband generation are often quite small due to the weak optorotational coupling. The normalized amplitudes (in logarithmic form) of upper and lower sum-sideband generation as a function of the frequency of the first probe field δ_a are shown in Fig. 2 under different pump powers of the control field. The parameters used in the calculation are chosen from Ref. [22]. It has been shown in Fig. 2(a) that the maximum amplitude of upper

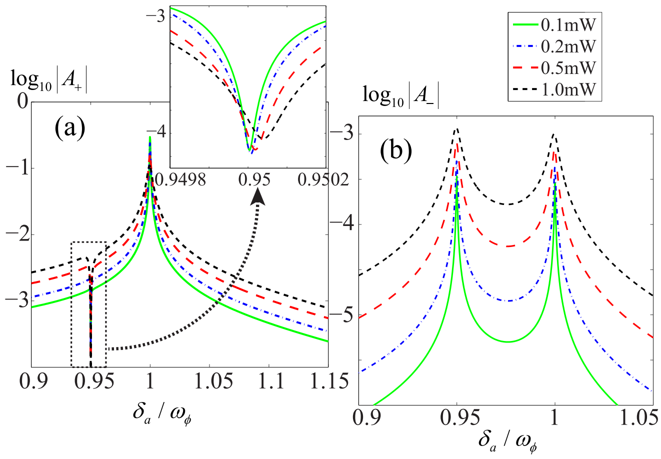

FIG. 2. The normalized amplitudes (in logarithmic form) of (a) upper and (b) lower sum sideband generation as a function of δ_a under different control fields. The parameters of the Laguerre-Gaussian optorotational system are [22] $m = 100\,\mathrm{ng}$, $\kappa_\phi/2\pi = 140.0\,\mathrm{Hz}$, $\omega_\phi/2\pi = 10.0\,\mathrm{MHz}$, $P_a = P_b = 100\,\mu\mathrm{W}$, $L = 1\,\mathrm{mm}$, $R = 10\,\mu\mathrm{m}$, $\kappa_a/2\pi = 10.0\,\mathrm{MHz}$, $l = 100$, and $\Delta = -\omega_\phi$. We set $\delta_b = 0.05\omega_\phi$, and the wavelength of the control field is chosen to be 810 nm here.

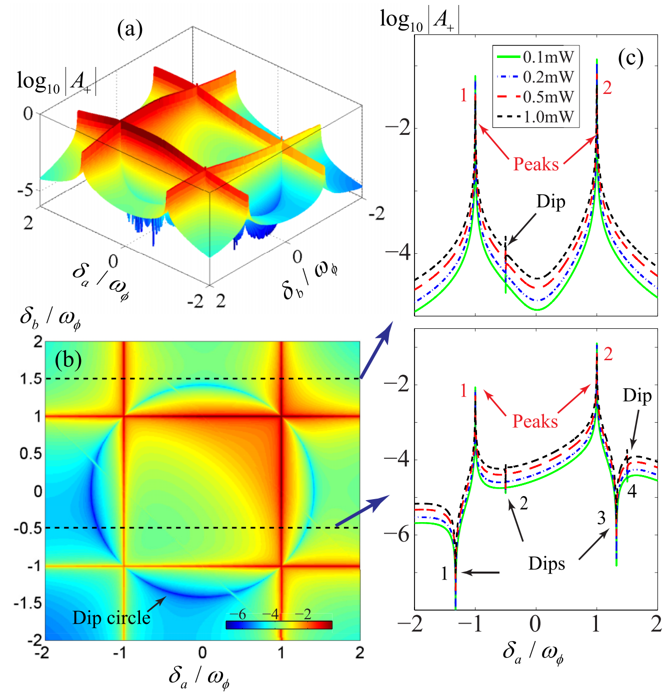

FIG. 3. The normalized amplitude (in logarithmic form) of upper sum-sideband generation vs δ_a and δ_b. (a) The surface plot and (b) the contour plot with the pump power $P_l = 1.0\,\mathrm{mW}$. (c) The normalized amplitudes of upper sum sideband generation vary with δ_a for different δ_b. We use $\delta_b = 1.5\omega_\phi$ (above) and $\delta_b = -0.5\omega_\phi$ (below). (d) Enlarged view of the contour plot near the cross point. (e) The normalized amplitudes of upper sum-sideband generation exhibits a peak instead of a dip at the cross point. The other parameters are the same as Fig. 2.

sum-sideband generation can reach $|A_+| \approx 0.1$, which corresponds to a power of about 10 μW and a power efficiency of about 10%. In general, the normalized amplitude of the upper sum-sideband generation increases monotonically with the increase of the pump power of the control field. However, some exceptions have been observed near the point of resonance due to the weak interference between multiple scattering paths. A typical example is shown in the partial enlarged drawing of Fig. 2(a), where the blue line (corresponding to the pump power of 0.2 mW) is located below the green line (corresponding to the pump power of 0.1 mW) near the resonance point $\delta_a = 0.95$. The amplitude of the lower sum-sideband generation is much smaller than the amplitude of the upper one under equivalent conditions. As shown in Fig. 2(b), the maximum amplitude of the lower sum-sideband generation is about $|A_-| \approx 10^{-3}$, which corresponds to a power of about 1 nW and a power efficiency of about 0.001%. The normalized amplitude of the lower sum-sideband generation also increases monotonically with the increase of the pump power of the control field, and no exception has been observed near the point of resonance.

There is a high dependence of Laguerre-Gaussian sum-sideband generation on the detuning between the control field and the two probe fields. Calculation results for the normalized amplitudes (in logarithmic form) of sum sideband generation as functions of both detuning δ_a and δ_b are shown in Figs. 3 and 4, where the normalized amplitudes of sum-sideband generation exhibit peak and dip structure for some specific combinations of δ_a and δ_b. These specific combinations of detuning are the so-called matching conditions [30], and the efficiencies of Laguerre-Gaussian sum-sideband generation can be enhanced or reduced significantly when the suitable matching conditions are met. From Fig. 2(a), we can identify that the amplitude of upper sum-sideband generation achieves the maximum at $\delta_a = \omega_\phi$ (the main peak) while it achieves the minimum at $\delta_a = 0.95\omega_\phi$ (the narrow dip). In Fig. 2(b), the amplitude of lower sum-sideband generation achieves the local maximum at both $\delta_a = \omega_\phi$ and $\delta_a = 0.95\omega_\phi$. The matching condition $\delta_a = \omega_\phi$ originates from the mechanical resonance of the torsional pendulum. The value 0.95 in these matching conditions comes from the parameter setting $\delta_b = 0.05\omega_\phi$ used in the calculation, and we confirm that the amplitude of upper sum-sideband generation achieves the minimum at $\delta_a + \delta_b = \omega_\phi$.

The surface plot for the normalized amplitude of upper sum-sideband generation [shown in Fig. 3(a)] exhibits orthogonal crisscross structure, where the peak values are located on the lines $\delta_a = \pm\omega_\phi$ and $\delta_b = \pm\omega_\phi$. Careful examination confirms that Fig. 3(a) is symmetrical for δ_a and δ_b due to the equal status of both detuning in the Laguerre-Gaussian sum-sideband generation, and one can identify clearly a circular structure in which the normalized amplitude of upper sum-sideband generation achieves local minimum [so-called dip circle; see the blue circular shown in Fig. 3(b)]. The physical interpretation for the dip circle is the π phase difference between the rotational responses to the two probe fields, which leads to the destructive interference for the upper sum-sideband generation in the optorotational system [40].

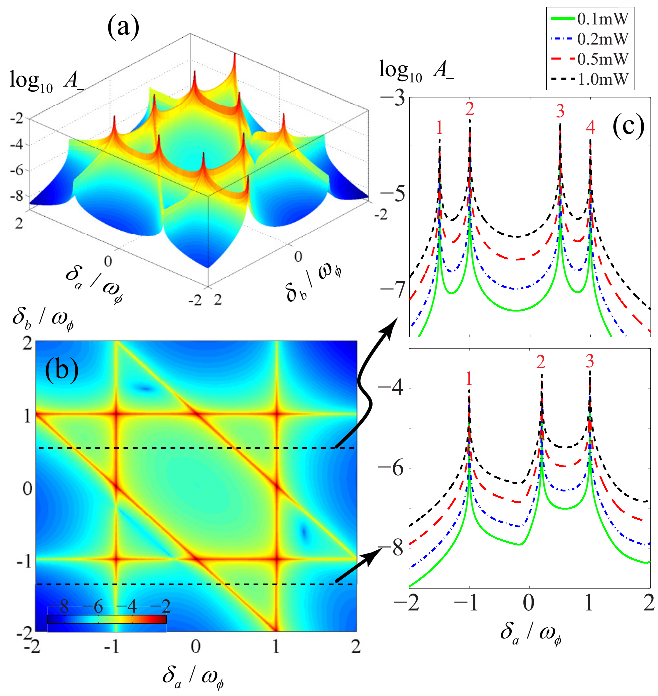

FIG. 4. The normalized amplitude (in logarithmic form) of lower sum-sideband generation vs δ_a and δ_b. (a) The surface plot and (b) the contour plot with the pump power $P_1 = 1.0$ mW. (c) The normalized amplitudes of upper sum-sideband generation vary with δ_a for different δ_b. We use $\delta_b = 0.5\omega_\phi$ (above) and $\delta_b = -1.4\omega_\phi$ (below). The other parameters are the same as Fig. 2.

From the analytical expression (5), the amplitude of the upper sum sideband generation can be rewritten as

$$\begin{aligned} a_s^+ &= a_s^{+(1)} + a_s^{+(2)}, \\ a_s^{+(1)} &= -\frac{(a_a^+\phi_b + a_b^+\phi_a)\tau(\Omega)}{i\hbar g^2|a_0|^2 - \theta(-\Omega)\tau(\Omega)}, \\ a_s^{+(2)} &= -\frac{i\hbar g^2 a_0\wp}{i\hbar g^2|a_0|^2 - \theta(-\Omega)\tau(\Omega)}, \end{aligned} \tag{6}$$

where the term $a_s^{+(1)}$ describes the one-step scattering into the upper sum sideband from the probe fields while $a_s^{+(2)}$ two-step scattering into the upper sum sideband from the control field. In general, the two-step scattering is much weaker than the one-step scattering. After some derivation, we obtain

$$a_s^{+(1)} \propto a_a^+ a_b^+ \tau(\Omega)[\tau(\delta_a) + \tau(\delta_b)], \tag{7}$$

where $\tau(\delta_a)$ and $\tau(\delta_b)$ can be seen as the susceptibilities of the rotational responses to the two probe fields. The one-step scattering into the upper sum sideband is determined by the total susceptibility $\tau(\delta_a) + \tau(\delta_b)$ and the sum susceptibility $\tau(\Omega)$. In the certain parameter regime $\kappa_\phi \ll \omega_\phi$, the total susceptibility $\tau(\delta_a) + \tau(\delta_b) \approx 0$ requires

$$I\left(\omega_\phi^2 - \delta_a^2 - i\kappa_\phi\delta_a\right) + I\left(\omega_\phi^2 - \delta_b^2 - i\kappa_\phi\delta_b\right) \approx 0, \tag{8}$$

which leads to the condition $\delta_a^2 + \delta_b^2 = 2\omega_\phi^2$. This condition is exactly the dip circle observed in Fig. 3(b). The sum susceptibility $\tau(\Omega) \approx 0$ requires

$$I\left(\omega_\phi^2 - \Omega^2 - i\kappa_\phi\Omega\right) \approx 0, \tag{9}$$

which leads to the condition $\Omega = \pm\omega_\phi$ or equivalently $\delta_a + \delta_b = \pm\omega_\phi$. This condition is exactly the dip observed in Fig. 2(a).

These matching conditions can be confirmed quantificationally. The normalized amplitudes of upper sum-sideband generation vary with δ_a for different δ_b are shown in Fig. 3(c). In the above subplot, $\delta_b = 1.5\omega_\phi$ is used, and we see two peaks located at $\delta_a = \omega_\phi$ and $\delta_a = -\omega_\phi$, due to the mechanical resonance of the torsional pendulum. A dip located at $\delta_a = -0.5\omega_\phi$ can be observed which corresponds to the $\delta_a + \delta_b = \omega_\phi$. The matching condition $\delta_a + \delta_b = -\omega_\phi$ results in $\delta_a = -2.5\omega_\phi$, which is out of parameter range $\delta_a \in [-2\omega_\phi, 2\omega_\phi]$. Due to the fact that $\delta_b^2 = 2.25\omega_\phi^2 > 2\omega_\phi^2$, the equation $\delta_a^2 + \delta_b^2 = 2\omega_\phi^2$ has no real solution for the detuning δ_a, which excludes the dip located at the dip circle. So we can know that there are two peaks and one dip for the upper sum-sideband generation in the parameter range $\delta_a \in [-2\omega_\phi, 2\omega_\phi]$. In the below subplot shown in Fig. 3(c), $\delta_b = -0.5\omega_\phi$ is used, and two peaks located at $\delta_a = \omega_\phi$ and $\delta_a = -\omega_\phi$ can be clearly observed. The matching condition $\delta_a + \delta_b = \pm\omega_\phi$ results in two dips located at $\delta_a = -0.5\omega_\phi$ and $\delta_a = 1.5\omega_\phi$ [labeled as dips 2 and 4 in the below subplot of Fig. 3(c)]. The matching condition $\delta_a^2 + \delta_b^2 = 2\omega_\phi^2$ has two real solutions for the case $\delta_b = -0.5\omega_\phi$, viz. $\delta_a/\omega_\phi = \pm\sqrt{7}/2 \approx 1.323$, which leads to two deep dips located at $\delta_a = -1.323\omega_\phi$ and $\delta_a = 1.323\omega_\phi$ [labeled as dips 1 and 3 in the below subplot of Fig. 3(c)]. So we can know that there are two peaks and four dips for the upper sum-sideband generation in the parameter range $\delta_a \in [-2\omega_\phi, 2\omega_\phi]$.

The surface plot for the normalized amplitude of lower sum-sideband generation is shown in Fig. 4(a), which exhibits a "sea-island" structure that the amplitude of lower sum-sideband generation is remarkable in the area of the island. We can identify three matching conditions for the lower sum-sideband generation, viz. $\delta_a = \pm\omega_\phi$, $\delta_b = \pm\omega_\phi$, $\delta_a + \delta_b = \pm\omega_\phi$, which corresponds to the orange lines shown in Fig. 4(b), and the islands are located at the intersection of these lines. The physical interpretation of the matching conditions for lower sum-sideband generation can be understood through the mechanical susceptibility, that the mechanical oscillation of the torsional pendulum becomes significant if the beating between the control field and one of the probe fields has a resonance with the mechanical eigenfrequency, and consequently leads to remarkable signals at the lower sum sideband via Stokes scattering of the cavity fields.

The matching conditions for lower sum-sideband generation have be confirmed quantificationally in Fig. 4(c). In the above subplot, $\delta_b = 0.5\omega_\phi$ is used, and we see two peaks located at $\delta_a = \omega_\phi$ [labeled as peak 4 in the above subplot of Fig. 4(c)] and $\delta_a = -\omega_\phi$ (labeled as peak 2), according to the matching condition $\delta_a = \pm\omega_\phi$. From the another matching condition $\delta_a + \delta_b = \pm\omega_\phi$, we can obtain $\delta_a/\omega_\phi = -0.5 \pm 1$, which results in two additional peaks located at $\delta_a = -1.5\omega_\phi$ (labeled as peak 1) and $\delta_a = 0.5\omega_\phi$ (labeled as peak 3). The total peaks add up to four in this case. In the blow subplot shown in Fig. 4(c), $\delta_b = -1.4\omega_\phi$ is used, there are two fixed

TABLE I. Matching conditions of Laguerre-Gaussian sum-sideband generation for achieving maximum and minimum.

	Conditions of achieving peaks	Conditions of achieving dips
Upper sum-sideband generation	$\delta_a = \pm\omega_\phi,\ \delta_b = \pm\omega_\phi$	$\delta_a + \delta_b = \pm\omega_\phi,\ \delta_a^2 + \delta_b^2 = 2\omega_\phi^2$
Lower sum-sideband generation	$\delta_a = \pm\omega_\phi,\ \delta_b = \pm\omega_\phi,\ \delta_a + \delta_b = \pm\omega_\phi$	

peaks located at $\delta_a = \omega_\phi$ (labeled as peak 3) and $\delta_a = -\omega_\phi$ (labeled as peak 1), according to the matching condition $\delta_a = \pm\omega_\phi$. The matching condition $\delta_a + \delta_b = -\omega_\phi$ results in the peak located at $\delta_a = 0.4\omega_\phi$ (labeled as peak 2). The matching condition $\delta_a + \delta_b = \omega_\phi$ results in $\delta_a = 2.4\omega_\phi$, which is out of parameter range $\delta_a \in [-2\omega_\phi, 2\omega_\phi]$. We can know that there are three peaks for the lower sum sideband generation in the parameter range $\delta_a \in [-2\omega_\phi, 2\omega_\phi]$, as we have observed in the blow subplot of Fig. 4(c).

Based on the discussion, the matching conditions for Laguerre-Gaussian sum-sideband generation are summarized in Table I. In what follows, we will discuss the influence of topological charge l on Laguerre-Gaussian sum-sideband generation, which provides another control parameter.

The normalized amplitudes of Laguerre-Gaussian sum sideband generation versus δ_a and δ_b with different topological charges are shown in Fig. 5, where the matching conditions are maintained for different topological charges. The topological charge l influences Laguerre-Gaussian sum-sideband generation on the width of the peaks and dips, viz. the line width shown in Fig. 5. For upper sum-sideband generation [Fig. 5(a)], the matching conditions $\delta_a = \pm\omega_\phi$ and $\delta_b = \pm\omega_\phi$ can be easily recognized, as well as the dip circle. The matching condition $\delta_a + \delta_b = \pm\omega_\phi$ can be confirmed clearly in an enlarged figure. The widths of the peaks and dips are about $0.02\omega_\phi$ for $l = 50$, while $0.05\omega_\phi$ for $l = 200$. In addition to influencing the width of the peaks and dips, the Laguerre-Gaussian mode with a high topological charge l leads to an overall improvement for the sum-sideband generation. As shown in Fig. 5(b), the amplitude of lower sum-sideband generation went up by several orders of magnitude [the color change in the sea area]. To show the improvement of the sum-sideband generation more accurately, we plot the normalized amplitude of upper sum-sideband generation under different topological charges in Fig. 5(c). As expected, the peak width becomes wider as the topological charge l increases, and there is an overall improvement for the normalized amplitude ($\log_{10}|A_+|$ increases by about 2/3 for topological charge l double; see the interval between the lines). However, there is a saturation effect for the peak value of the normalized amplitude [see the peak values for different topological charges l in Fig. 5(c)], which limits further improvement of the sum-sideband generation.

The relationship between the Laguerre-Gaussian sum-sideband generation and the Laguerre-Gaussian second-order sideband generation is checked, and it is found that there is a fixed relation between the degenerate and the nondegenerate cases, in a sense similar to the basic sum frequency and second-order harmonic generation by a nonlinear crystal [34]. In the degenerate case, viz. $\delta_a = \delta_b = \delta$, we have $a_i^+ = s_i\Theta(\delta)$, $a_i^- = s_i^*\Xi(\delta)$, and $\phi_i = \hbar g a_0^* a_i^+/\tau(\delta) = \hbar g a_0^* s_i\Theta(\delta)/\tau(\delta)$ for the subscript $i = a, b$, with $\Theta(\delta) = \tau(\delta)/[\theta(-\delta)\tau(\delta) - \alpha]$, $\alpha = i\hbar g^2|a_0|^2$, and $\Xi(\delta) = i\hbar g^2 a_0^2\Theta^*(\delta)/[\tau^*(\delta)\theta(\delta)]$. After some calculations, we can obtain the amplitude of the degenerate sum-sideband generation ($\delta_a = \delta_b = \delta$) as follows:

$$\begin{aligned} a_s^+ &= 2s_a s_b \frac{\frac{a_0^*}{\tau(\delta)\tau(2\delta)}\Theta^2(\delta) + iga_0\Xi^*(\delta)\Theta(\delta)\left[1 - \frac{\alpha}{\tau(\delta)\theta^*(2\delta)}\right]}{\theta(-2\delta)\tau(2\delta) - ig|a_0|^2} \\ &\equiv 2s_a s_b\mathcal{E}(\delta), \end{aligned} \tag{10}$$

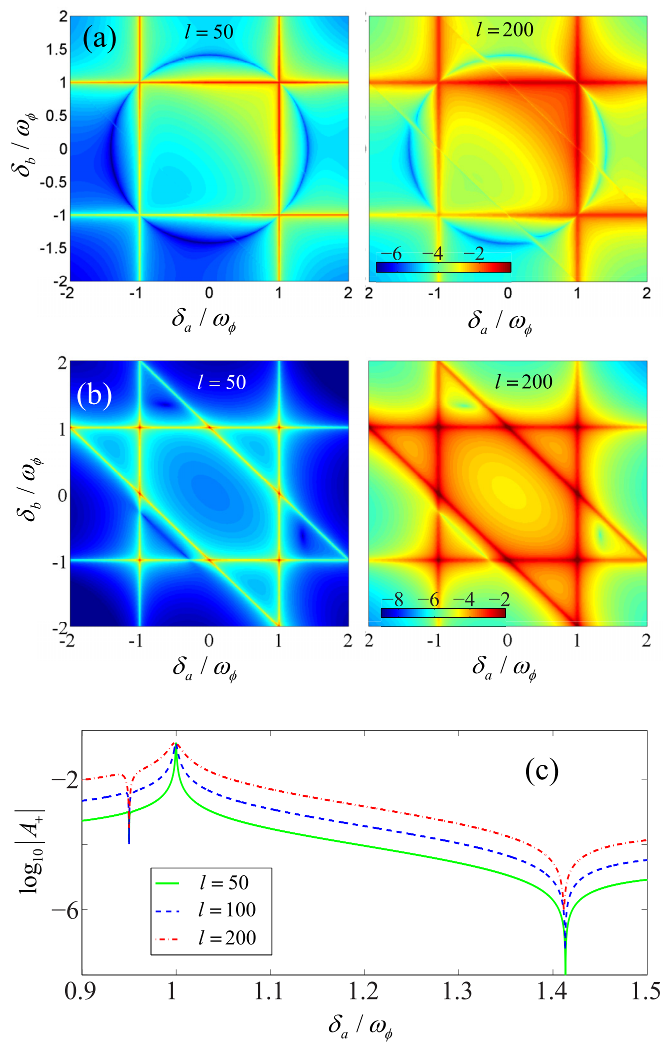

FIG. 5. The contour plots of the normalized amplitudes (in logarithmic form) of (a) upper and (b) lower sum-sideband generation with different topological charge l. (c) The normalized amplitude of upper sum-sideband generation as a function of δ_a under different topological charge l. We use the pump power $P_l = 1.0$ mW, and the other parameters are the same as Fig. 2.

where $s_i^2\mathcal{E}(\delta)$ is exactly the amplitude of the second-order sideband generation [21], which establish a relation between the degenerate and the nondegenerate cases.

Finally, we give some discussion on the feasibility of experimentally observing the effects based on the current experimental progresses. In the present work, the parameters of the Laguerre-Gaussian optorotational system are chosen from a previous work [22]: $m = 100\,\text{ng}$, $\kappa_\phi/2\pi = 140.0\,\text{Hz}$, $\omega_\phi/2\pi = 10.0\,\text{MHz}$, $L = 1\,\text{mm}$, $R = 10\ \ \mu\text{m}$, $\kappa_a/2\pi = 10.0\,\text{MHz}$, and $l = 100$. Through sustained effort, high-l Laguerre-Gaussian modes can be achieved readily in experiments via spiral phase elements [12], and the azimuthal structure of laser beams can be modified via reflection or transmission from the spiral phase elements. Here we consider the configuration used in Ref. [16], which provides complete self-consistent conditions for intracavity Laguerre-Gaussian mode buildup. With the development of nanotechnology, the spiral phase mirrors can be produced by direct machining of an aluminum disk surface with an ultraprecision point diamond turning lathe [16,41]. For example, the Nanotech 250UPL lathe has a feedback resolution of 34 pm [16,41], which is sufficiently precise to create suitable spiral phase elements for the implementation of our results (in the spatial scale of a few μm). We also note that the spiral phase plate and mirror can be fabricated with high precision and low mass (sub-μg), and the generation of LG beams with a topological charge value as high as 1000 has been demonstrated [12]. In addition, the mechanical oscillators (torsional pendulum) with high-quality factor (mechanical quality factors exceeding $Q_m = 10^8$), low mass (with an effective mass $m_{\text{eff}} = 27$ pg), and high frequency (a few MHz) has been realized in experiments [42], which may provide other alternative devices for the implementation of our results.

IV. CONCLUSION

In summary, Laguerre-Gaussian optical sum-sideband generation via orbital angular momentum exchange has been studied in an optorotational system beyond the linearized approach. The analytical expressions describing the amplitude of the upper and lower sum sidebands are obtained. To make Laguerre-Gaussian sum-sideband generation observable and controllable within the experimentally available parameter range, the features of Laguerre-Gaussian sum-sideband generation in an optorotational system are discussed in detail, including the pump power dependence, matching conditions, and the role of the topological charge value l. We show that Laguerre-Gaussian sum-sideband generation can be remarkable even at low power through the satisfaction of matching conditions. These matching conditions for Laguerre-Gaussian sum-sideband generation are summarized, and the physical interpretation of matching conditions is discussed. The role of the topological charge value l on the sum-sideband generation exhibits a saturation effect for the peak value of the normalized amplitude, and consequently limits further improvement of the Laguerre-Gaussian sum-sideband generation. This investigation may provide further insight into the understanding of the optorotational system with orbital angular momentum exchange and find applications in Laguerre-Gaussian optical frequency comb [43] and communications. In the current paper, for simplicity, we only consider the case that both control and probe fields are in the fundamental Gaussian modes. If the OAM of the control field is different from the OAM of the probe fields, or the two probe fields have different OAM, the OAM in these modes should affect the efficiency of the process, and the situation becomes very complicated. Further analysis is required to move in that direction.

ACKNOWLEDGMENTS

The work was supported by the National Key Research and Development Program of China (Grant No. 2016YFA0301203), the National Science Foundation of China (Grants No. 12022507, No. 11774113, and No. 11870529), and the Fundamental Research Funds for the Central Universities (Grant No. 2019kfyRCPY111).

[1] L. Allen, M. W. Beijersbergen, R. J. Spreeuw, and J. P. Woerdman, Orbital angular momentum of light and the transformation of Laguerre-Gaussian laser modes, Phys. Rev. A **45**, 8185 (1992).

[2] A. M. Yao and M. J. Padgett, Orbital angular momentum: Origins, behavior, and applications, Adv. Opt. Photon. **3**, 161 (2011).

[3] N. R. Heckenberg, R. McDuff, C. P. Smith, and A. White, Generation of optical phase singularities by computer-generated holograms, Opt. Lett. **17**, 221 (1992).

[4] J. Arlt, K. Dholakia, L. Allen, and M. J. Padgett, Parametric downconversion for light beams possessing orbital angular momentum, Phys. Rev. A **59**, 3950 (1999).

[5] M. W. Beijersbergen, R. Coerwinkel, M. Kristensen, and J. P. Woerdman, Helical-wavefront laser beams produced with a spiral phaseplate, Opt. Commun. **112**, 321 (1994).

[6] G. A. Turnbull, D. A. Roberson, G. M. Smith, L. Allen, and M. J. Padgett, Generation of free-space Laguerre-Gaussian modes at millimetre-wave frequencies by use of a spiral phaseplate, Opt. Commun. **127**, 183 (1996).

[7] A. Forbes, A. Dudley, and M. McLaren, Creation and detection of optical modes with spatial light modulators, Adv. Opt. Photon. **8**, 200 (2016).

[8] G. Gibson, J. Courtial, M. J. Padgett, M. Vasnetsov, V. Pas'ko, S. M. Barnett, and S. Franke-Arnold, Free-space information transfer using light beams carrying orbital angular momentum, Opt. Express **12**, 5448 (2004).

[9] L. Zhu and J. Wang, Arbitrary manipulation of spatial amplitude and phase using phase-only spatial light modulators, Sci. Rep. **4**, 7441 (2014).

[10] M. W. Beijersbergen, L. Allen, H. van der Veen, and J. P. Woerdman, Astigmatic laser mode converters and transfer of orbital angular momentum, Opt. Commun. **96**, 123 (1993).

[11] A. E. Willner, H. Huang, Y. Yan, Y. Ren, N. Ahmed, G. Xie, C. Bao, L. Li, Y. Cao, Z. Zhao, J. Wang, M. P. J. Lavery, M. Tur, S. Ramachandran, A. F. Molisch, N. Ashrafi, and S. Ashrafi,

Optical communications using orbital angular momentum beams, Adv. Opt. Photon. **7**, 66 (2015).

[12] Y. Shen, G. T. Campbell, B. Hage, H. Zou, B. C. Buchler, and P. K. Lam, Generation and interferometric analysis of high charge optical vortices, J. Opt. **15**, 044005 (2013).

[13] H. He, M. E. J. Friese, N. R. Heckenberg, and H. Rubinsztein-Dunlop, Direct Observation of Transfer of Angular Momentum to Absorptive Particles from a Laser Beam with a Phase Singularity, Phys. Rev. Lett. **75**, 826 (1995).

[14] M. F. Andersen, C. Ryu, P. Clade, V. Natarajan, A. Vaziri, K. Helmerson, and W. D. Phillips, Quantized Rotation of Atoms from Photons with Orbital Angular Momentum, Phys. Rev. Lett. **97**, 170406 (2006).

[15] G. Volpe and D. Petrov, Torque Detection Using Brownian Fluctuations, Phys. Rev. Lett. **97**, 210603 (2006).

[16] M. Bhattacharya and P. Meystre, Using a Laguerre-Gaussian Beam to Trap and Cool the Rotational Motion of a Mirror, Phys. Rev. Lett. **99**, 153603 (2007).

[17] M. Aspelmeyer, T. J. Kippenberg, and F. Marquardt, Cavity optomechanics, Rev. Mod. Phys. **86**, 1391 (2014).

[18] H. Xiong and Y. Wu, Fundamentals and applications of optomechanically induced transparency, Appl. Phys. Rev. **5**, 031305 (2018).

[19] J.-X. Peng, Z. Chen, Q.-Z. Yuan, and X.-L. Feng, Optomechanically induced transparency in a Laguerre-Gaussian rotational-cavity system and its application to the detection of orbital angular momentum of light fields, Phys. Rev. A **99**, 043817 (2019).

[20] Z. Zhang, Y.-P. Wang, and X. Wang, Measuring orbital angular momentum of vortex beams in optomechanics, Front. Phys. **16**, 32503 (2021).

[21] S. H. Kazemi and M. Mahmoudi, Optomechanical second-order sideband effects in a Laguerre-Gaussian rotational cavity system, Phys. Scr. **95**, 045107 (2020).

[22] M. Bhattacharya, P.-L. Giscard, and P. Meystre, Entanglement of a Laguerre-Gaussian cavity mode with a rotating mirror, Phys. Rev. A **77**, 013827 (2008).

[23] H.-J. Cheng, S.-J. Zhou, J.-X. Peng, A. Kundu, H.-X. Li, L. Jin, and X.-L. Feng, Tripartite entanglement in a Laguerre-Gaussian rotational-cavity system with an yttrium iron garnet sphere, J. Opt. Soc. Am. B **38**, 285 (2021).

[24] C. K. Law, Interaction between a moving mirror and radiation pressure: A Hamiltonian formulation, Phys. Rev. A **51**, 2537 (1995).

[25] H. Xiong, L.-G. Si, A.-S. Zheng, X. Yang, and Y. Wu, Higher-order sidebands in optomechanically induced transparency, Phys. Rev. A **86**, 013815 (2012).

[26] H. Xiong, Y.-W. Fan, X. Yang, and Y. Wu, Radiation pressure induced difference-sideband generation beyond linearized description, Appl. Phys. Lett. **109**, 061108 (2016).

[27] S. Weis, R. Riviere, S. Deléglise, E. Gavartin, O. Arcizet, A. Schliesser, and T. J. Kippenberg, Optomechanically induced transparency, Science **330**, 1520 (2010).

[28] Y. Jiao, H. Lü, J. Qian, Y. Li, and H. Jing, Nonlinear optomechanics with gain and loss: Amplifying higher-order sideband and group delay, New J. Phys. **18**, 083034 (2016).

[29] S. Huang and A. Chen, Fano resonance and amplification in a quadratically coupled optomechanical system with a Kerr medium, Phys. Rev. A **101**, 023841 (2020).

[30] H. Xiong, L.-G. Si, X.-Y. Lü, and Y. Wu, Optomechanically induced sum sideband generation, Opt. Express **24**, 5773 (2016).

[31] X.-Y. Wang, L.-G. Si, X.-H. Lu, and Y. Wu, Generation and enhancement of sum sideband in a quadratically coupled optomechanical system with parametric interactions, Opt. Express **27**, 29297 (2019).

[32] W.-A. Li and G.-Y. Huang, Enhancement of optomechanically induced sum sidebands using parametric interactions, Phys. Rev. A **100**, 023838 (2019).

[33] W.-L. Xu, Y.-P. Gao, T.-J. Wang, and C. Wang, Magnon-induced optical high-order sideband generation in hybrid atom-cavity optomagnonical system, Opt. Express **28**, 22334 (2020).

[34] H. Xiong, L.-G. Si, J. F. Guo, X.-Y. Lu, and X. Yang, Classical theory of cylindrical nonlinear optics: Second-harmonic generation, Phys. Rev. A **83**, 063845 (2011).

[35] B. Wang, Z.-X. Liu, C. Kong, H. Xiong, and Y. Wu, Magnon-induced transparency and amplification in *PT*-symmetric cavity-magnon system, Opt. Express **26**, 20248 (2018).

[36] Z.-X. Liu, B. Wang, C. Kong, H. Xiong, and Y. Wu, Magnetic-field-dependent slow light in strontium atom-cavity system, Appl. Phys. Lett. **112**, 111109 (2018).

[37] Z.-X. Liu, C. You, B. Wang, H. Xiong, and Y. Wu, Phase-mediated magnon chaos-order transition in cavity optomagnonics, Opt. Lett. **44**, 507 (2019).

[38] S. Liu, B. Liu, and W.-X. Yang, Highly sensitive mass detection based on nonlinear sum-sideband in a dispersive optomechanical system, Opt. Express **27**, 3909 (2019).

[39] H. Xiong, Z. X. Liu, and Y. Wu, Highly sensitive optical sensor for precision measurement of electrical charges based on optomechanically induced difference-sideband generation, Opt. Lett. **42**, 3630 (2017).

[40] S. Rao and Y. Huang, Generation and enhancement of sum sideband in a parity-time-symmetric optomechanical system, J. Phys. B **53**, 155403 (2020).

[41] L. Li, Y. Y. Allen, C. Huang, D. A. Grewell, A. Benatar, and Y. Chen, Fabrication of diffractive optics by use of slow tool servo diamond turning process, Opt. Eng. **45**, 113401 (2006).

[42] H. Kaviani, R. Ghobadi, B. Behera, M. Wu, A. Hryciw, S. Vo, D. Fattal, and P. Barclay, Optomechanical detection of light with orbital angular momentum, Opt. Express **28**, 15482 (2020).

[43] I. S. Maksymov and A. D. Greentree, Coupling light and sound: Giant nonlinearities from oscillating bubbles and droplets, Nanophotonics **8**, 367 (2019).